



Green synthesis of core–shell gold–palladium@palladium nanocrystals dispersed on graphene with enhanced catalytic activity toward oxygen reduction and methanol oxidation in alkaline media

Jie-Ning Zheng^a, Shan-Shan Li^a, Xiaohong Ma^b, Fang-Yi Chen^a, Ai-Jun Wang^{a,*}, Jian-Rong Chen^a, Jiu-Ju Feng^{a,*}

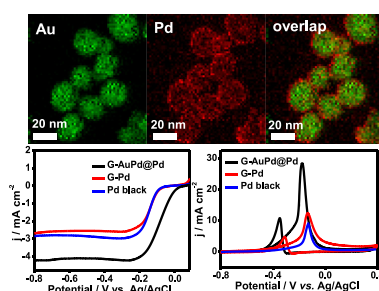
^a College of Geography and Environmental Science, College of Chemistry and Life Science, Zhejiang Normal University, Jinhua 321004, China

^b State Key Laboratory of Multiphase Complex Systems, Institute of Process Engineering, Chinese Academy of Sciences, Beijing 100190, China

HIGHLIGHTS

- AuPd@Pd nanocrystals are prepared by a simple and green wet-chemical method.
- HEPES is used as a reducing and a shape-directing agent.
- The AuPd@Pd nanocrystals are dispersed on graphene by ultrasonication.
- The nanocomposites show high electrocatalytic activity toward ORR and MOR in alkaline media.

GRAPHICAL ABSTRACT



ARTICLE INFO

Article history:

Received 25 January 2014

Received in revised form

25 March 2014

Accepted 26 March 2014

Available online 2 April 2014

Keywords:

Graphene

Core–shell

Oxygen reduction reaction

Methanol oxidation

ABSTRACT

Well-defined core–shell gold–palladium@palladium nanocrystals (AuPd@Pd) are facilely prepared by a simple and green wet-chemical method at 25 °C. A Good's buffer, 2-[4-(2-hydroxyethyl)-1-piperazinyl] ethanesulfonic acid (HEPES), is used as a reducing agent and a shape-directing agent, while there is no template, seed, organic solvent, or surfactant involved. The AuPd@Pd nanocrystals are uniformly dispersed on graphene nanosheets by ultrasonication, resulting in the formation of graphene supported AuPd@Pd (G-AuPd@Pd). The as-prepared nanocomposites exhibit the improved catalytic activity, good tolerance, and better stability for oxygen reduction reaction (ORR) and methanol oxidation reaction (MOR) in alkaline media, compared with the G-Pd and commercial Pd black catalysts. The as-developed method may provide a promising pathway for large-scale fabrication of AuPd-based catalysts.

© 2014 Elsevier B.V. All rights reserved.

1. Introduction

Direct methanol fuel cells (DMFCs) have attracted enormous attention, owing to their high energy density, easy operation, and

* Corresponding authors.

E-mail addresses: ajwang@zjnu.cn (A.-J. Wang), jjfeng@zjnu.cn, jjfengnju@gmail.com (J.-J. Feng).

low handling temperature [1,2]. There are two major reaction processes occurred, namely methanol oxidation reaction (MOR) on the anode and oxygen reduction reaction (ORR) on the cathode, where Pt and Pt-based materials have been extensively investigated as both anode and cathode catalysts in acid media [3,4]. However, the high cost and scarce resources of Pt have hindered their promising commercial applications. Additionally, the Pt-based electrocatalysts are easily poisoned by chemisorbed CO-like intermediates in acid media [5]. Alternatively, the

kinetics will be greatly improved in alkaline media, where Pt-free catalysts can be used [6]. Moreover, the relatively cheap and more abundant Pd is a good alternative for both ORR and MOR in alkaline media, as verified in the literature [7,8].

Besides, the enhanced catalytic performance by incorporating a second metal (M) into Pd (Pd–M) is attributed to the synergistic effects and rich diversity of the compositions [9]. Recently, a variety of Pd–M nanomaterials have been prepared, including Pd–Pt [10,11], Pd–Au [12,13], Pd–Ag [14,15], and Pd–Ni [5,16] alloyed nanostructures. These catalysts displayed the improved catalytic activity for ORR or MOR in alkaline media. For example, Feng and co-workers synthesized Pd–Pt nanodendrites with the enhanced electrocatalytic activity for methanol oxidation, compared with commercial Pd black and Pt black catalysts [17]. Chen et al. fabricated hollow PdNi nanoparticles with the higher catalytic activity than that of the commercial Pd/C toward ORR [18].

Among the numerous synthesized bimetallic nanocrystals, Au–Pd nanoparticles are very fascinating for their high catalytic activity [19]. To date, many efforts have been devoted to fabricating different Au–Pd nanostructures, such as Au@Pd core–shell nanoparticles [12], hollow Au–Pd nanostructures [20], and spherical Au–Pd alloys [21]. Although these nanostructures showed good catalytic performance in fuel cells, their catalytic features for both ORR and MOR in alkaline media were seldom investigated. Moreover, their large-scale commercial applications were severely constrained. This is due to the preparation of AuPd nanoparticles closely dependent on surfactant or organic agents, along with severe reaction conditions. For example, AuPd nanoparticles were fabricated at 340 °C in the presence of octylether, oleylamine, 1,2-hex-adekanediol, and oleic acid [22]. In another example, hollow AuPd nanocrystals were prepared by galvanic displacement using the pre-prepared Ag nanoparticles at 160 °C as the template [20]. High reaction temperature, special experimental apparatus or complex reaction system are not good for large-scale preparation. Therefore, it is always desired to develop a simple and green method to synthesize AuPd nanoparticles in a large scale at 25 °C, without any seed, organic solvent, or surfactant.

Moreover, the bimetallic nanoparticles tend to agglomerate during their repeated use in catalysis [23]. This issue can be efficiently overcome by the development of graphene science [24], because graphene has a large specific surface area, two dimensional nanostructures, good electrical conductivity, and unique chemical property [25,26]. Recently, graphene is widely used as a good support for loading metal catalysts such as Pt [27], Pd [28], PtCo [29], and PtPd [30] catalysts.

Herein, we demonstrate a seedless, simple, and green method for preparation of Pd decorated AuPd core–shell nanostructures (AuPd@Pd) at 25 °C, just using a Good's buffers of 2-[4-(2-hydroxyethyl)-1-piperazine-yl] ethanesulfonic acid (HEPES) as a reducing agent and a shape-directing agent [31]. The as-prepared nanoparticles are uniformly loaded on graphene nanosheets (G–AuPd@Pd) and examined as an electrocatalyst for ORR and MOR, using graphene supported Pd dendrites (G–Pd) and commercial Pd black catalysts as references.

2. Experimental section

2.1. Chemicals

Graphite powder (8000 meshes), palladium chloride (PdCl_2), chlorauric acid (HAuCl_4), HEPES, and commercial Pd black were purchased from Aladdin Company (Shanghai, China). Other chemicals were of analytical grade and used without further purification. All the aqueous solutions were prepared with twice-distilled water in the whole experiments.

2.2. Preparation of graphene

The GO was prepared from natural graphite powder through acid-oxidation based on a modified Hummers' method [32]. The thickness and lateral dimension of the GO nanosheets was about 1.1–1.4 nm and 150 nm to 9 μm , respectively. For preparation of graphene, 5 mg of the as-prepared GO was dispersed in 5 mL of water via ultrasonication, resulting in a homogeneous yellow-brown aqueous suspension, followed by the addition of 3 mL of freshly prepared 0.01 M NaBH_4 . The solution color quickly changed to black.

2.3. Synthesis of the G–AuPd@Pd

The aqueous solution of HEPES (100 mM) was initially prepared, and the pH value was adjusted to 7.4 ± 0.1 by adding freshly prepared 1 M NaOH [31]. Next, 6.72 mL of water was put into 2 mL of the above HEPES solution, followed by simultaneously putting into 1.03 mL of HAuCl_4 (24.28 mM) and 0.25 mL of PdCl_2 (100 mM). Notably, the concentrations of the HEPES, HAuCl_4 , and PdCl_2 solutions are 50, 2.5, and 2.5 mM, respectively. Without shaking, the mixed solution color changed from purple red to dark green, and finally to black within 10 min. The final products were collected by centrifugation, and washed thoroughly with water.

For preparation of the G–AuPd@Pd, 10 mL of the as-prepared AuPd@Pd suspension was mixed with 5 mL of the above graphene suspension under ultrasonication. Control experiments were performed only using HAuCl_4 or PdCl_2 as a precursor, while other conditions were kept unchanged. The as-obtained products were denoted as G–Au or G–Pd accordingly.

2.4. Characterization

The morphology and chemical compositions of the samples were determined by JEM-2100F high resolution transmission electron microscopy (HR-TEM) coupled with an energy-dispersive X-ray spectrometer (EDS, Dxford-1NCA) at an acceleration voltage of 200 kV. High angle annular dark-field scanning TEM (HAADF-STEM) imaging and elemental mappings were examined on a scanning transmission electron microscope (STEM). The oxidation states were determined on a K-Alpha X-ray photoelectron spectroscopy (XPS, ThermoFisher, E. Grinstead, UK) with an Al $K\alpha$ X-ray radiation (1486.6 eV) for excitation. The crystal structures were characterized by the powder X-ray diffraction (XRD) pattern (Rigaku Dmax-2000 diffractometer) using Cu $K\alpha$ radiation ($\lambda = 0.15418$ nm). The UV–vis absorption spectra were acquired on a Lambda950 UV/Vis/NIR spectrometer. Fourier transform infrared (FT-IR) analysis was conducted in the form of KBr pellets with a Nicolet 670 FT-IR spectrometer. Raman experiments were performed on a Renishaw Raman system model 1000 spectrometer equipped with a CCD detector, performed with a He/Ne laser at a wavelength of 633 nm. Thermogravimetric analysis (TGA) was carried out in air, using NETZSCH STA 449C thermogravimetric analyzer. The samples were heated from 25 °C to 900 °C at the heat rate of 10 K min^{-1} .

2.5. Electrochemical measurements

The electrochemical measurements were performed on a CHI832b electrochemical workstation (CH Instruments, Chenhua Co., Shanghai, China) at 25 °C. A three-electrode system was used for all electrochemical experiments, which included a platinum wire as the counter electrode, an Ag/AgCl electrode as

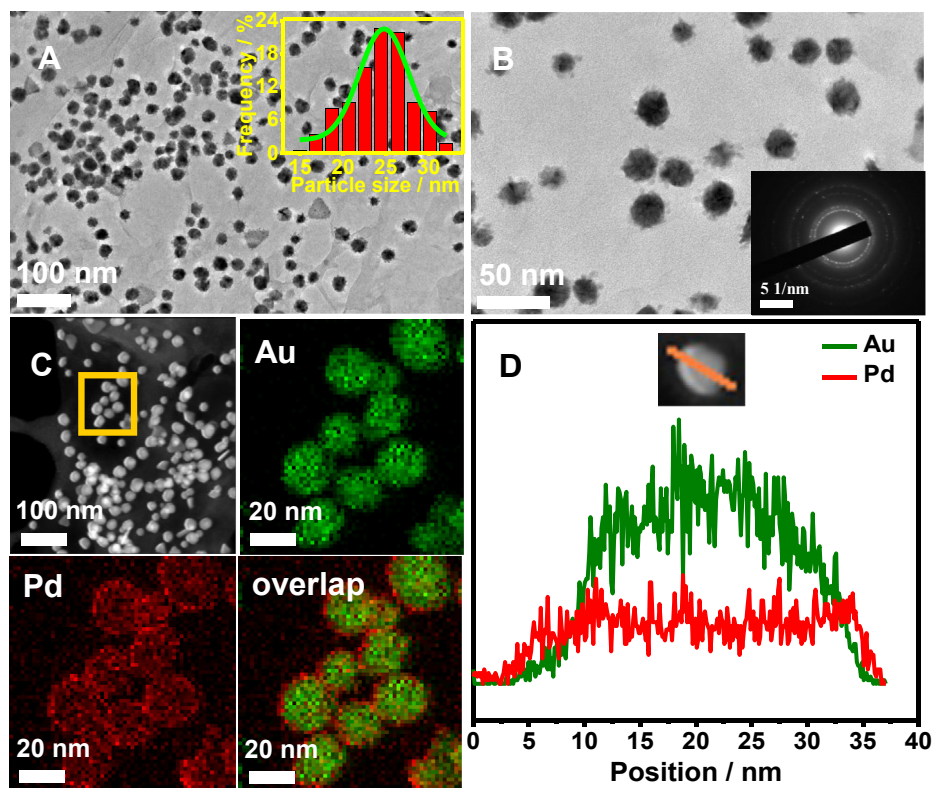


Fig. 1. (A, B) TEM and (C) HAADF-STEM-EDS mapping images of the G-AuPd@Pd. (D) HAADF-STEM image and cross-sectional compositional line profiles of a single AuPd@Pd nanoparticle. Insets show the corresponding size distribution in image (A) and SAED pattern in (B).

the reference electrode, and the sample modified glassy carbon electrode (GCE) as the working electrode. Rotating disk electrode (RDE) experiments were conducted at the Gamry's RDE (616) with a glassy carbon disk (4 mm in diameter). All the potentials in this work were expressed with respect to the Ag/AgCl electrode.

For preparation of the G-AuPd@Pd (the metal proportion is 78.6 wt%), 6.0 mg of the typical sample was dropped into 3.0 mL of water to form a homogeneous suspension by ultrasonication for approximately 30 min. Then, 6 and 10 μL of the suspensions were uniformly dropped onto the electrode surfaces of the GCE and RDE, and dried in air, followed by covering a layer of 4 and 6 μL of Nafion ionomers (0.05 wt%), respectively. The G-Pd (the metal proportion is 33.0 wt%), G-Au (the metal proportion is 52.8 wt%) and commercial Pd black catalysts modified electrodes were prepared in the similar way. In addition, the Pd loading is about 0.09 mg cm^{-2} for the G-AuPd@Pd, 0.06 mg cm^{-2} for the G-Pd, and 0.03 mg cm^{-2} for the commercial Pd black catalysts modified electrodes, respectively.

CO-stripping voltammograms were obtained by oxidizing pre-adsorbed CO (CO_{ad}) in 0.5 M H_2SO_4 at the scan rate of 50 mV s^{-1} . CO was bubbled for 30 min to allow complete adsorption of CO onto the catalysts. The working electrode was maintained at -0.1 V , and excess CO in the electrolyte was removed by purging with N_2 for 30 min.

The ORR polarization curves were recorded in oxygen-saturated 0.1 M KOH with a sweep rate of 5 mV s^{-1} at different rotation speeds ranging from 100 to 2500 rpm. The Koutecky–Levich plots obtained by using the inverse current density (j^{-1}) as a function of the inverse of the square root of the rotation rate ($\omega^{-1/2}$) at -0.7 V . The slopes of the linear fitting lines are used to calculate the number of transferred electrons (n) according to the Koutecky–Levich equation:

$$\frac{1}{i} = \frac{1}{i_k} + \frac{1}{i_d} = \frac{1}{i_k} + \frac{1}{B\omega^{1/2}} \quad (2)$$

$$B = 0.2nFC_0D_0^{2/3}\nu^{-1/6} \quad (3)$$

where i is the measured current, i_k is the kinetic current, i_d is the diffusion-limiting current, ω is the rotate speed, n is the number of the transferred electrons, F is the Faraday constant ($96,485 \text{ C mol}^{-1}$), C_0 is the oxygen solubility ($1.110^{-3} \text{ mol L}^{-1}$), D_0 is the oxygen diffusivity ($1.9 \times 10^{-5} \text{ cm}^2 \text{ s}^{-1}$), and ν is the kinetic viscosity of the electrolyte ($0.01 \text{ cm}^2 \text{ s}^{-1}$) [33]. By putting these parameters into the equation (3), $B = 0.0376 \text{ n}$. And B factor can be calculated from the as-mentioned slopes. The electrocatalytic activity and stability tests were conducted by cyclic voltammetry and chronoamperometry in 1.0 M KOH, accordingly, using MOR as a model system.

3. Results and discussion

As shown by the low magnification TEM image (Fig. 1A), the product contains a lot of uniform spherical nanocrystals, with an average diameter of 24.4 nm (inset in Fig. 1A), which are homogeneously dispersed on the surfaces of graphene nanosheets. The corresponding EDS analysis confirms the coexistence of Au and Pd elements (Fig. S1, Supporting information). Besides, the atomic ratio of Au to Pd is 52.85:47.15, which is similar to the stoichiometric ratio (1:1) of the precursors. Besides, the GO was successfully exfoliated into nanosheets via ultrasonic treatment, clearly displaying the flake-like shapes of the GO nanosheets (Fig. S2, Supporting information).

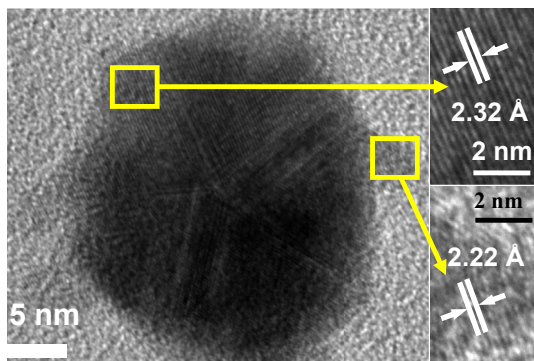


Fig. 2. HR-TEM images of an individual AuPd@Pd nanoparticle.

Furthermore, each nanoparticle is decorated by plenty of tiny grains, as strongly supported by the medium magnification TEM image (Fig. 1B), in which a dark inner core and a discontinuous shell with light color assembled by many smaller nanoparticles, indicating the formation of core–shell nanostructures on the surfaces of graphene nanosheets. Furthermore, polycrystalline nature of the Au–Pd hybrid nanocrystals was demonstrated by the SAED pattern (inset in Fig. 1B).

Importantly, HAADF-STEM-EDS mapping images (Fig. 1C) clearly manifest the formation of the core–shell AuPd@Pd nanostructures. The Au alloyed with relatively less Pd content is mainly distributed in the interior of the nanoparticles, whereas much more Pd content is detected at the outside edge. As revealed by the corresponding elemental line scanning analysis (Fig. 1D), the core–shell nanoparticle is constituted of alloyed AuPd as a core and pure Pd self-assembled by many tiny Pd grains as a shell, which are expected to be good for the improved catalytic performance of a catalyst [34,35].

For comparison, the morphology features of the home-made G-Au, G-Pd, and commercial Pd black samples are also elucidated by TEM analysis (Fig. S3A–C, Supporting information). It can

be observed the metallic nanoparticles in G-Au (Fig. S3A, Supporting information) and G-Pd (Fig. S3B, Supporting information) samples are dendritic in shape and homogeneously dispersed on the RGO nanosheets without obvious agglomeration. Their morphology features are quite different from the commercial Pd black sample that contains many spherical tiny particles (Fig. S3C, Supporting information). The average particle sizes are obtained from their histograms, with the values of around 38.39 for the G-Au, 36.53 for the G-Pd, and 18.55 nm for the Pd black samples, respectively. Additionally, the corresponding size distributions are 30.40–47.9 nm, 30.59–43.20 nm, and 10.89–28.68 nm, accordingly.

To have deep insight on the microstructural information of the AuPd@Pd nanoparticles, HR-TEM images (Fig. 2) illustrate the fine crystalline and continuous lattice fringes marked from the AuPd core to Pd shell in a single AuPd@Pd particle. The d-spacing value of the adjacent fringes is calculated to be 2.32 Å for the core, which are close to AuPd alloy with a value of 2.30 Å [36]. Furthermore, the lattice spacing is coincidentally located between pure Au (2.355 Å, JCPDS-04-0784) and Pd (2.246 Å, JCPDS-46-1043), confirming the formation of the AuPd alloy. Meanwhile, the lattice spacing of 2.22 Å in the shell corresponds to the (111) planes of Pd [37]. Additionally, the AuPd core is decahedral and five-fold twinned, indicating that its surface is enclosed by the (111) facets [38].

The oxidation states and compositions of the G-AuPd@Pd were determined by XPS measurements (Fig. 3). The XPS survey spectrum (Fig. 3A) illustrates the signals from Au, Pd, O, and C elements, revealing the formation of the G-AuPd@Pd. Further detail information is provided by high-resolution XPS spectra of Au 4f and Pd 3d via fitting the peaks (Fig. 3B and C). Clearly, the oxidation state of Au is zero valence, confirming the formation of metallic Au [39], while those of Pd are assigned to metallic Pd and Pd²⁺ ions [17]. These results suggest the ease reduction of AuCl₄[−] ions to Au atoms, owing to much higher reduction potential of AuCl₄[−]/Au (1.002 V) than that of Pd²⁺/Pd (0.591 V). Notably, the oxygen-containing functional groups such as C–O, C=O, and O–C=O groups in the graphene (Fig. 3D) remarkably decrease, compared with the

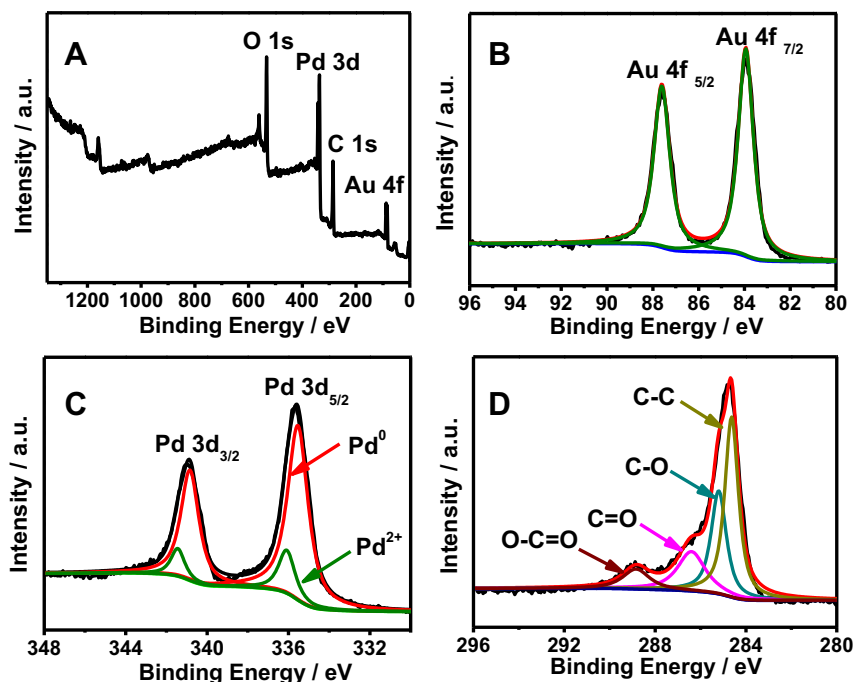


Fig. 3. (A) Survey, (B) high-resolution Au 4f, (C) Pd 3d, and (D) C 1s XPS spectra of the G-AuPd@Pd.

original GO (Fig. S4, Supporting information), indicating the efficient reduction of the GO to graphene [40].

XRD analysis is a facile and important tool to check crystalline materials. As displayed in Fig. 4A, the XRD pattern of the G-AuPd@Pd is provided, in which the four diffraction peaks correspond to the (111), (200), (220), and (311) planes of the face-centered cubic (fcc) structure of metal. For comparison, XRD spectra of the G-Au, G-Pd nanomaterials, and bulk Au (JCPDS-04-0784) are provided. Clearly, the peak positions of the G-AuPd@Pd are similar to those of the G-Au and bulk Au, rather than the G-Pd. This is attributed to very thin thickness of the Pd shell and much less amount of Pd in the core that have nearly no contribution to the diffraction peaks [41]. In addition, the most intensive peak of GO at around 11.0° corresponds to the (002) planes with the interlayer spacing of 0.85 nm. This value is much larger than that of the pristine graphite (0.34 nm), owing to the

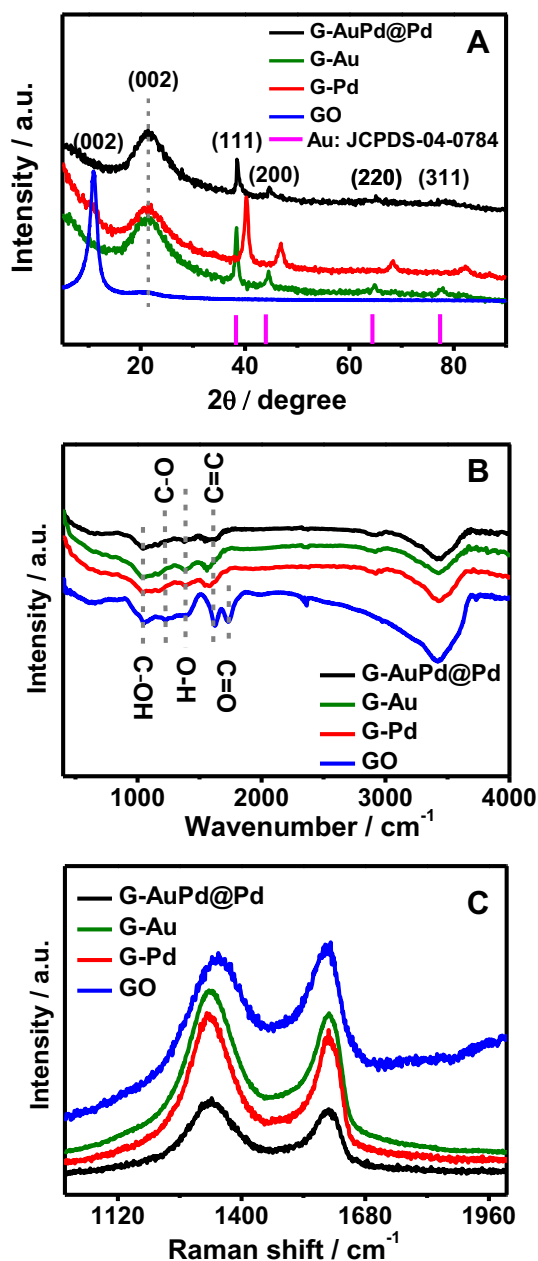


Fig. 4. (A) XRD, (B) FT-IR, and (C) Raman spectra of the G-AuPd@Pd, G-Au, G-Pd, and GO samples.

intercalated oxygenated functional groups between layers [42]. For the G-AuPd@Pd, G-Pd, and G-Au, the intensity of the diffraction peaks of the (002) planes decreases and shift to the higher angle at 21.4° , indicating the effective reduction of GO to graphene by NaBH_4 [43].

UV–vis spectroscopy is a feasible tool to characterize the G-AuPd@Pd in the aqueous solution (Fig. S5, Supporting information). For the G-Au, a distinct absorption peak at 554 nm is ascribed to the surface plasmon resonance of Au [44]. Alternatively, no pronounced characteristic peak is detected for the G-AuPd@Pd or G-Pd under the same conditions. We speculate that the thin Pd shell has the ability to strongly damp out the surface plasmon resonance from the Au core [34], strongly demonstrating the formation of the core–shell AuPd@Pd particles. The UV–vis spectra are further confirmed the effective reduction of GO by the great changes before and after the reduction with NaBH_4 . Specifically, for the initial GO, the strong peak at 228 nm and the smaller shoulder peak at 297 nm are assigned to the $\pi \rightarrow \pi^*$ transition of the aromatic C–C bond and the $n \rightarrow \pi^*$ transition of the C=O bond [11], respectively. After reduction and further decoration with metallic nanocrystals, the absorption peak at 228 nm red shifts to 255 nm for the G-AuPd@Pd, G-Au, and G-Pd, similar to that of the graphene. It indicates that GO is significantly deoxygenated and graphene is efficiently formed in the nanocomposites [42], as demonstrated by the FT-IR test with the sharp decrease of the main stretching peaks from the C–OH, C–O, O–H, and C=O groups (Fig. 4B) [45].

This assumption is well consistent with the data from Raman spectroscopy (Fig. 4C). The typical D and G bands correspond to the A_{1g} breathing mode of the disordered graphite structure and the doubly degenerate E_{2g} of graphite [46], respectively. The corresponding peak intensity ratios (I_D/I_G) are 1.24, 1.22, and 1.02 for the G-AuPd@Pd, G-Pd, and G-Au, respectively, using the GO ($I_D/I_G = 0.66$) as a reference. These results demonstrate the formation of smaller in-plane sp^2 domains during the reduction of GO and again confirm the formation of graphene [40]. Impressively, the G band shifts to the longer-wavelength for the G-metal hybrids, with the value of around 4 cm^{-1} . This phenomenon should be attributed to the enhanced electric conductivity using graphene as a support and good electrical conductivity of the AuPd@Pd alloys, along with their synergetic effects [47].

The TGA/DSC analysis confirms the good thermal stability of the G-AuPd@Pd (Fig. 5, curve a). For each sample, the weight loss at about 100, 200, and 500 $^\circ\text{C}$ is assigned to the removal of water molecules absorbed between the graphene nanosheets, the pyrolysis of oxygen-containing functional groups, and the combustion of the carbon skeleton to CO or CO_2 [48,49], respectively. The G-AuPd@Pd displays small weight drops under the same conditions,

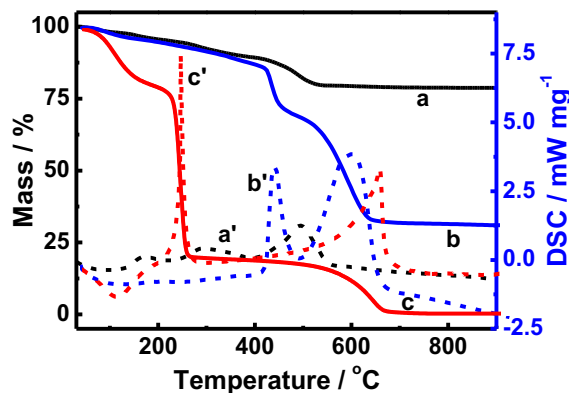


Fig. 5. TGA curves of the G-AuPd@Pd (curve a), G-Pd (curve b), and GO (curve c) samples. The DSC curves of the G-AuPd@Pd (curve a'), G-Pd (curve b'), and GO (curve c').

similar to that of the G-Pd (curve b) and G-Au (Fig. S6, Supporting information), but it is greatly different from that of the GO (curve c). These results demonstrate the decrease of the oxygen-containing functional groups in the graphene, further revealing efficient reduction of GO in the present synthesis. In addition, the metal loading is 78.6 wt% for the G-AuPd@Pd (evaluated via the residual mass), which is larger than those of the G-Pd (33.0 wt%) and G-Au (52.8 wt%).

As well known, the hydrogen can diffuse into the Pd bulk to form Pd hydride, instead of adsorbing onto the Pd surface, and so it is not rational to calculate the electrochemically active surface area (EASA) of the catalyst based on the hydrogen adsorption/desorption method. Alternatively, CO-stripping measurements are good candidates for estimating the EASA of the Pd-based catalysts. The EASA can be estimated based on the following Equation (1) [11]:

$$\text{EASA} = \frac{Q}{m \times C} \quad (1)$$

where Q is the charge for CO desorption–electrooxidation, m is the loading amount of Pd, and C ($420 \mu\text{C cm}^{-2}$) [50] is the charge needed for the adsorption of a CO monolayer. The EASA values are $93.5 \text{ m}^2 \text{ g}^{-1}_{\text{Pd}}$ for the G-AuPd@Pd (Fig. 6A), $71.9 \text{ m}^2 \text{ g}^{-1}_{\text{Pd}}$ for the G-Pd (Fig. 6B), and $7.25 \text{ m}^2 \text{ g}^{-1}_{\text{Pd}}$ (Fig. 6C) for the Pd black catalyst, respectively.

Fig. 7A shows the cyclic voltammograms of the G-AuPd@Pd, G-Pd, and Pd black catalysts modified electrodes in N_2 -saturated $0.5 \text{ M H}_2\text{SO}_4$ at a scan rate of 50 mV s^{-1} . Clearly, all the catalysts display well-defined hydrogen desorption/adsorption peaks and preoxidation/reduction peaks. In the positive scan, hydrogen desorption emerges in the potential window of -0.2 to 0 V , and the hydroxyl species (OH_{ad}) adsorption appears beyond 0.4 V . In the negative sweep, the OH_{ad} are reduced from 0.4 to 0.5 V , and hydrogen is below 0 V . Evidently, the adsorption and desorption peaks of the hydroxyl species shift positively on the G-AuPd@Pd, compared with the G-Pd and Pd black catalysts, revealing weak affinity of the hydroxyl species on the surface of the G-AuPd@Pd. The shift is benefit to ORR and MOR [51], indicating that the Au core could improve their resistance to oxidation. Moreover, there is no characteristic peak associated with hydrogen desorption/adsorption for the G-Au sample (Fig. S7, Supporting information), because pure Au has negligible catalytic activity for hydrogen adsorption [52].

The ORR measurements were performed in O_2 -saturated 0.1 M KOH at a rotation rate of 1600 rpm . Fig. 7B shows the typical polarization curves of the G-AuPd@Pd, G-Pd, and Pd black catalysts modified electrodes. In each case, the diffusion limiting currents are observed below -0.30 V , whereas the mixed kinetic-diffusion controlled region appears from -0.20 to 0 V . The current densities are normalized with respect to the geometrical area of the modified electrode. The G-AuPd@Pd shows a more positive onset potential (-0.01 V), compared with those of the G-Pd (-0.09 V) and Pd black (-0.11 V) catalysts. Besides, the half-wave potentials of the G-AuPd@Pd, G-Pd, and Pd black catalysts are -0.09 , -0.14 , and -0.15 V , respectively. These results reveal the improved catalytic activity of the G-AuPd@Pd. Moreover, the onset potential is much positive for the G-AuPd@Pd, compared with the core-shell Au@Pd (-0.14 V) in the literature [53], owing to the better support of graphene and the alloyed feature of the AuPd@Pd nanostructures. Additionally, similar catalytic behavior toward ORR is observed for the Pd black catalyst, as manifested in the literature [54].

It is known that the kinetic current density (i_k) represents the intrinsic electrocatalytic activity of a catalyst. The Pd mass kinetic activity is obtained by normalizing the kinetic current densities

against the Pd mass of these catalysts (Fig. 7C). It is found that the G-AuPd@Pd displays the significantly enhanced mass kinetic activity in the kinetic-diffusion controlled region (from -0.05 to -0.15 V).

Besides, Fig. 7D provides the specific activity (which is normalized to the real Pd surface area) and mass activity at -0.15 V . The G-AuPd@Pd shows the specific activity of $0.401 \text{ mA cm}^{-2}_{\text{Pd}}$, which is 3.8 and 1.1 times higher than those of the G-Pd ($0.105 \text{ mA cm}^{-2}_{\text{Pd}}$) and Pd black ($0.368 \text{ mA cm}^{-2}_{\text{Pd}}$) catalysts. Furthermore, the specific activity of the G-AuPd@Pd is higher than the nanoporous PdNi alloys (0.210 mA cm^{-2}) [55] and Pt-on-Pd nanodendrites (0.307 mA cm^{-2}) [35] reported previously. Similarly, the mass activity of the G-AuPd@Pd is $0.174 \text{ mA } \mu\text{g}^{-1}_{\text{Pd}}$, which is 2.2 and 8.9 times larger than those of the G-Pd ($0.080 \text{ mA } \mu\text{g}^{-1}_{\text{Pd}}$) and Pd black ($0.195 \text{ mA } \mu\text{g}^{-1}_{\text{Pd}}$) catalysts.

More detailed investigations of the ORR kinetic parameters on the G-AuPd@Pd, G-Pd, and Pd black catalysts modified electrodes were performed by altering the rotation speed (100 – 2500 rpm) at a

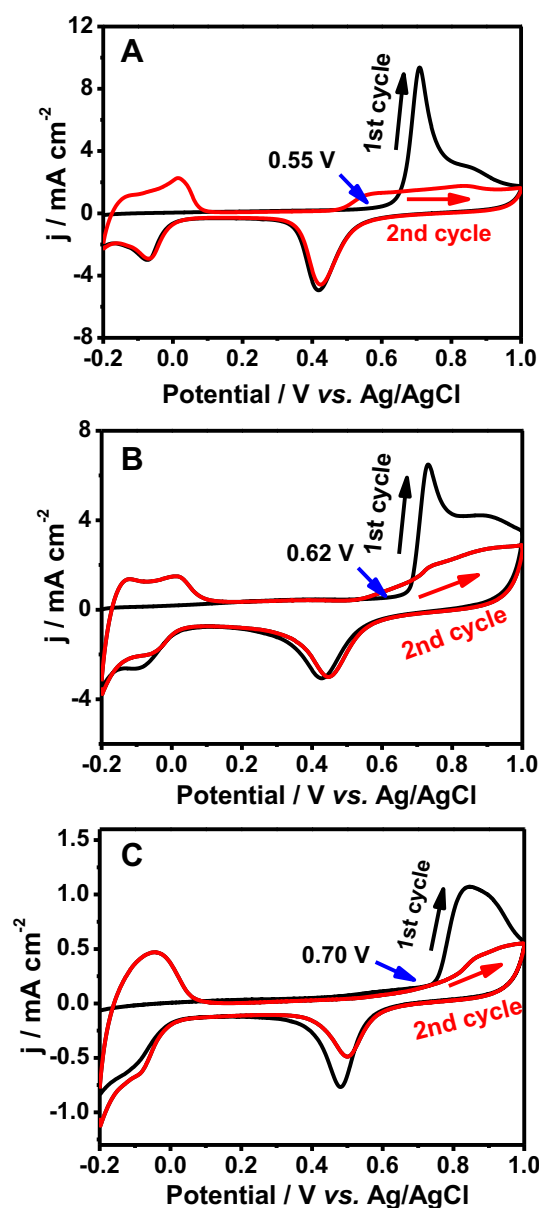


Fig. 6. CO-stripping voltammograms of the G-AuPd@Pd (A), G-Pd (B), and commercial Pd black (C) catalysts in $0.5 \text{ M H}_2\text{SO}_4$ at a scan rate of 50 mV s^{-1} .

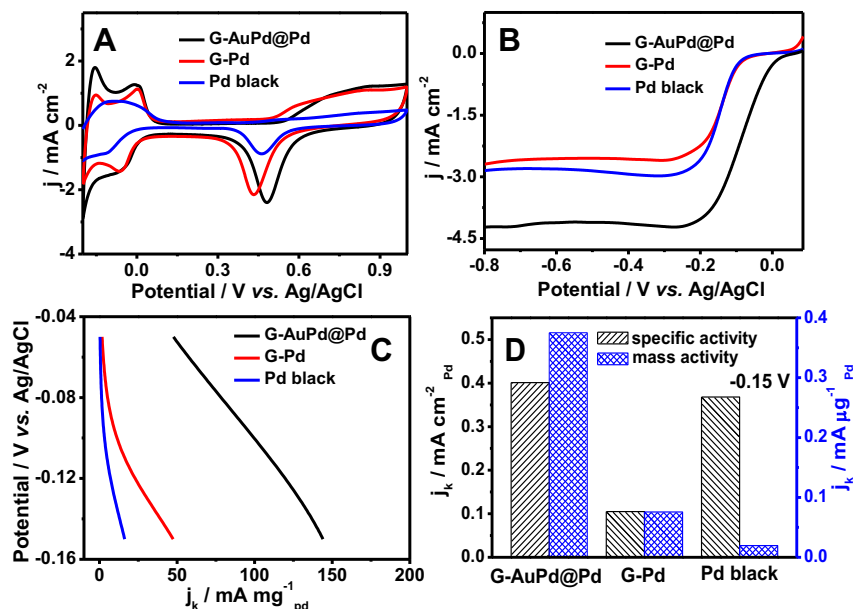


Fig. 7. (A) Cyclic voltammograms of the G-AuPd@Pd, G-Pd, and Pd black catalysts modified electrodes in N_2 -saturated 0.5 M H_2SO_4 at a scan rate of 50 mV s⁻¹. (B) ORR polarization curves of the G-AuPd@Pd, G-Pd, and Pd black catalysts modified electrodes in O_2 -saturated 0.1 M KOH at 1600 rpm with a scan rate of 5 mV s⁻¹. (C) The corresponding mass kinetic current density at different potentials, and (D) specific kinetic current densities and mass kinetic current densities at -0.15 V.

scan rate of 5 mV s⁻¹ (Fig. 8A–C). As illustrated in Fig. 8D, the electron transfer number is calculated to be 4.0, 3.65, and 3.73 for the G-AuPd@Pd, G-Pd, and Pd black at -0.7 V, respectively, verifying the efficient reduction of O_2 to H_2O via the four-electron pathway, unlike that of the G-Au without any effect on the ORR (Fig. S8, Supporting information).

The catalytic activity of the G-AuPd@Pd modified electrode was investigated by cyclic voltammetry in 1.0 M KOH containing 1.0 M methanol at a scan rate of 50 mV s⁻¹ (Fig. 9A). And the

current values were normalized to the geometrical area of the modified electrode. There are two distinct peaks observed in the forward and backward scanning, which are assigned to methanol oxidation and the removal of incompletely oxidized carbonaceous species, respectively. It is found that the current density of the G-AuPd@Pd is higher than those of the G-Pd and Pd black catalysts under the identical conditions. And the catalytic current density for the Pd black catalyst is similar to those reported in the literature [17,56].

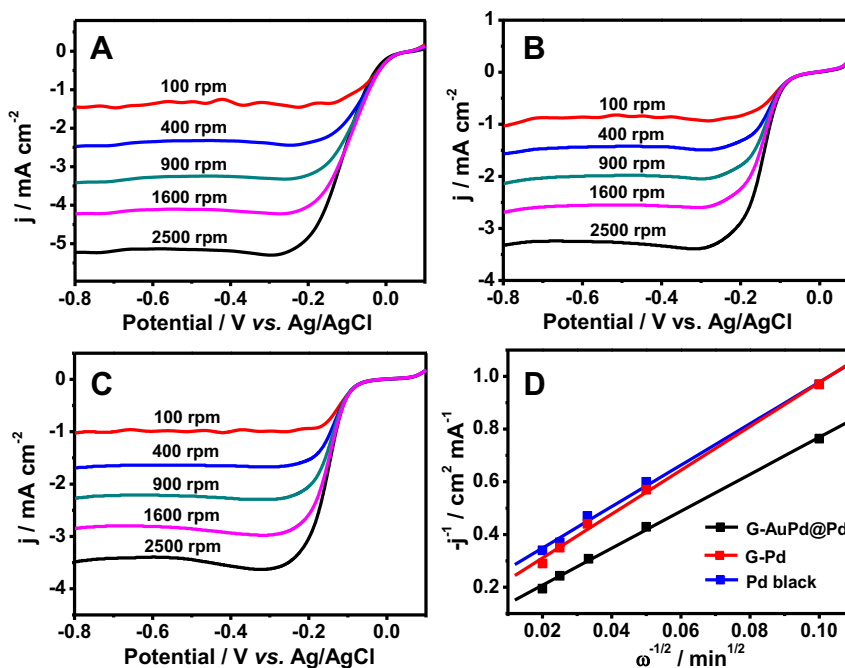


Fig. 8. (A) Polarization curves of ORR on the (A) G-AuPd@Pd, (B) G-Pd, and (C) Pd black catalysts modified electrodes in O_2 -saturated 0.1 M KOH at different rotation rates at a scan rate of 5 mV s⁻¹. (D) The electron transfer number (n) of the G-AuPd@Pd, G-Pd, and Pd black catalysts modified electrodes at -0.7 V.

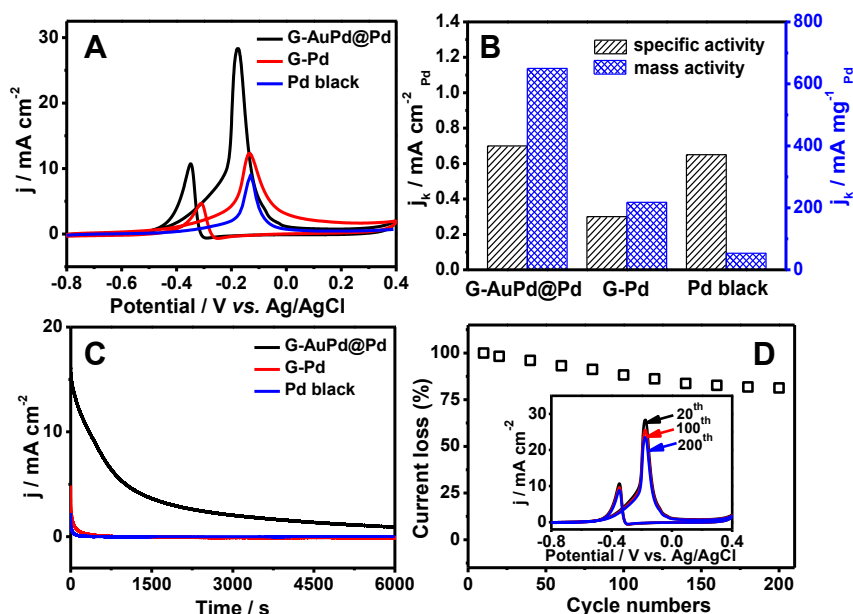


Fig. 9. (A) Cyclic voltammograms of the G-AuPd@Pd, G-Pd, and Pd black catalysts modified electrodes in 1.0 M KOH + 1.0 M methanol at a scan rate of 50 mV s⁻¹. (B) The corresponding specific activities, mass activities, and (C) chronoamperometric curves of the G-AuPd@Pd, G-Pd, and Pd black catalysts modified electrodes at a given potential of -0.15 V. (D) The forward peak current density (j) as a function of potential scanning cycles of the G-AuPd@Pd modified electrode. Inset shows the corresponding 20th, 100th, and 200th cyclic voltammograms.

Fig. 9B shows the corresponding specific and mass activity. The G-AuPd@Pd shows the highest specific activity with a value of 0.695 mA cm⁻², which is 2.3 and 1.1 times higher than those of the G-Pd (0.303 mA cm⁻²) and Pd black (0.650 mA cm⁻²) catalysts, respectively. Moreover, the mass activity of the G-AuPd@Pd is 0.650 mA μg⁻¹ Pd, which is larger than those of the G-Pd (0.218 mA μg⁻¹ Pd) and Pd black (0.053 mA μg⁻¹ Pd) catalysts, respectively. It is noticed that the catalytic activity of the G-AuPd@Pd is higher than those of graphene-supported Pd (0.360 mA μg⁻¹ Pd) [45] and porous PdCu nanoparticles (0.363 mA μg⁻¹ Pd) [57].

Meanwhile, the onset anodic potential is -0.46 V for the G-AuPd@Pd, which is 100 and 70 mV more negative than those of the G-Pd (-0.36 V) and Pd black (-0.39 V) catalysts, respectively. Moreover, there is no anodic peak appeared in the case of the G-Au sample (Fig. S9, Supporting Information), indicating the inactivity of Au for MOR. These results manifest the easier oxidation of methanol with the G-AuPd@Pd.

The catalytic activity and stability of the G-AuPd@Pd were determined by chronoamperometry in 1.0 M KOH containing 1.0 M methanol (Fig. 9C). Upon applying a potential of -0.15 V for 6000 s, the initial and steady oxidation current densities of the G-AuPd@Pd are larger than those of the G-Pd and Pd black catalysts under the same conditions, further confirming the improved catalytic activity of the G-AuPd@Pd. Note that the initial current density decays more slowly for the G-AuPd@Pd, compared with those for the G-Pd and Pd black catalysts, verifying the better resistance of the G-AuPd@Pd to the CO-like intermediates.

The good stability of the G-AuPd@Pd is further confirmed by the cyclic voltammetry measurements, in which the electrocatalytic current density is almost kept constant within 200 cycles (Fig. 9D). Specifically, using the peak current density of the 20th cycle as a reference, the peak current density on the G-AuPd@Pd remains about 90.1% after 100 cycles and 83.0% after 200 cycles, respectively. These results again indicate the enhanced durability of the G-AuPd@Pd. Furthermore, the G-AuPd@Pd is remained almost unchanged after the durability test, as revealed by TEM image

(Fig. S10, Supporting information). These features should be responsible for the improved electrocatalytic stability of the G-AuPd@Pd.

The enhanced electrocatalytic performances of the G-AuPd@Pd are ascribed to the following three factors. (i) Synergetic effects between Au and Pd. The incorporated Au can oxidize the intermediates adsorbed onto the Pd active sites (Pd-CO) at a relatively lower potential via forming ambiguous Au-OH. And more Pd active sites are regenerated for the catalytic reaction [58]. (ii) The enlarged specific surface area is provided by the Pd shells assembled with many small grains, and more active sites are offered by abundant atomic steps, edges, and corner atoms located on the shell [59,60]. (iii) Graphene, as a support, can enlarge surface area, facilitate electron transfer, and prevent nanoparticles from agglomeration.

4. Conclusion

In summary, well-defined core-shell AuPd@Pd nanostructures were fabricated by a simple and green wet-chemical method, using HEPES as a reducing agent and a shape-directing agent. The as-prepared AuPd@Pd nanoparticles were well dispersed on the surfaces of graphene nanosheets via simple ultrasonication, and the resulting G-AuPd@Pd exhibited the enhanced catalytic activity for ORR and MOR in alkaline media, compared with the G-Pd and commercial Pd black catalysts. This is ascribed to the enlarged specific surface area, the synergetic effects between Au, Pd, and graphene. The developed approach can be used for preparing other efficient graphene-based electrocatalysts in DMFCs.

Acknowledgment

This work was financially supported by the National Natural Science Foundation of China (Nos. 21175118, 21275130 and 21275131), and Zhejiang province university young academic leaders of academic climbing project (No. pd2013055).

Appendix A. Supplementary data

Supplementary data related to this article can be found at <http://dx.doi.org/10.1016/j.jpowsour.2014.03.131>.

References

- [1] C.W. Xu, H. Wang, P.K. Shen, S.P. Jiang, *Adv. Mater.* 19 (2007) 4256–4259.
- [2] Y. Hu, H. Zhang, P. Wu, H. Zhang, B. Zhou, C. Cai, *Phys. Chem. Chem. Phys.* 13 (2011) 4083–4094.
- [3] N.M. Marković, T.J. Schmidt, V. Stamenković, P.N. Ross, *Fuel Cells* 1 (2001) 105–116.
- [4] E.A. Franceschini, M.M. Bruno, F.J. Williams, F.A. Viva, H.R. Corti, *ACS Appl. Mater. Interfaces* 5 (2013) 10437–10444.
- [5] Y. Zhao, X. Yang, J. Tian, F. Wang, L. Zhan, *Int. J. Hydrogen Energy* 35 (2010) 3249–3257.
- [6] C. Xu, L. Cheng, P. Shen, Y. Liu, *Electrochem. Commun.* 9 (2007) 997–1001.
- [7] M.H. Seo, S.M. Choi, H.J. Kim, W.B. Kim, *Electrochem. Commun.* 13 (2011) 182–185.
- [8] C. Zhu, S. Guo, S. Dong, *Chem. Eur. J.* 19 (2013) 1104–1111.
- [9] T. Ramulifho, K.I. Ozoemena, R.M. Modibedi, C.J. Jafra, M.K. Mathe, *Electrochim. Acta* 59 (2012) 310–320.
- [10] Y. Lu, Y. Jiang, W. Chen, *Nano Energy* 2 (2013) 836–844.
- [11] S.-S. Li, J.-J. Lv, Y.-Y. Hu, J.-N. Zheng, J.-R. Chen, A.-J. Wang, J.-J. Feng, *J. Power Sources* 247 (2014) 213–218.
- [12] L. Kuai, X. Yu, S. Wang, Y. Sang, B. Geng, *Langmuir* 28 (2012) 7168–7173.
- [13] Z. Liu, B. Zhao, C. Guo, Y. Sun, F. Xu, H. Yang, Z. Li, *J. Phys. Chem. C* 113 (2009) 16766–16771.
- [14] Y. Wang, Z.M. Sheng, H. Yang, S.P. Jiang, C.M. Li, *Int. J. Hydrogen Energy* 35 (2010) 10087–10093.
- [15] L. Jiang, A. Hsu, D. Chu, R. Chen, *Electrochim. Acta* 55 (2010) 4506–4511.
- [16] B. Li, J. Prakash, *Electrochem. Commun.* 11 (2009) 1162–1165.
- [17] J.-J. Lv, J.-N. Zheng, S.-S. Li, L.-L. Chen, A.-J. Wang, J.-J. Feng, *J. Mater. Chem. A* (2014) 4384–4390.
- [18] M. Wang, W. Zhang, J. Wang, D. Wexler, S.D. Poynton, R.C.T. Slade, H. Liu, B. Winther-Jensen, R. Kerr, D. Shi, J. Chen, *ACS Appl. Mater. Interfaces* 5 (2013) 12708–12715.
- [19] G.J. Hutchings, *Chem. Commun.* (2008) 1148–1164.
- [20] H.M. Song, D.H. Anjum, R. Sougrat, M.N. Hedhili, N.M. Khashab, *J. Mater. Chem.* 22 (2012) 25003–25010.
- [21] M. Nie, P.K. Shen, Z. Wei, *J. Power Sources* 167 (2007) 69–73.
- [22] H.M. Song, B.A. Moosa, N.M. Khashab, *J. Mater. Chem.* 22 (2012) 15953–15959.
- [23] J. Wang, G. Yin, H. Liu, R. Li, R.L. Flemming, X. Sun, *J. Power Sources* 194 (2009) 668–673.
- [24] X. Wang, D. Liu, S. Song, H. Zhang, *J. Am. Chem. Soc.* 135 (2013) 15864–15872.
- [25] M.J. McAllister, J.-L. Li, D.H. Adamson, H.C. Schniepp, A.A. Abdala, J. Liu, M. Herrera-Alonso, D.L. Milius, R. Car, R.K. Prud'homme, I.A. Aksay, *Chem. Mater.* 19 (2007) 4396–4404.
- [26] C. Tan, X. Huang, H. Zhang, *Mater. Today* 16 (2013) 29–36.
- [27] E. Yoo, T. Okata, T. Akita, M. Kohyama, J. Nakamura, I. Honma, *Nano Lett.* 9 (2009) 2255–2259.
- [28] H. Zhao, J. Yang, L. Wang, C. Tian, B. Jiang, H. Fu, *Chem. Commun.* 47 (2011) 2014–2016.
- [29] Q. Yue, K. Zhang, X. Chen, L. Wang, J. Zhao, J. Liu, J. Jia, *Chem. Commun.* 46 (2010) 3369–3371.
- [30] S. Guo, S. Dong, E. Wang, *ACS Nano* 4 (2009) 547–555.
- [31] J. Xie, J.Y. Lee, D.I.C. Wang, *Chem. Mater.* 19 (2007) 2823–2830.
- [32] N.I. Kovtyukhova, P.J. Ollivier, B.R. Martin, T.E. Mallouk, S.A. Chizhik, E.V. Buzaneva, A.D. Gorchinskiy, *Chem. Mater.* 11 (1999) 771–778.
- [33] J. Wu, H. Yang, *Nano Res.* 4 (2011) 72–82.
- [34] H. Wang, Z. Sun, Y. Yang, D. Su, *Nanoscale* 5 (2013) 139–142.
- [35] Z. Peng, H. Yang, *J. Am. Chem. Soc.* 131 (2009) 7542–7543.
- [36] J.W. Hong, Y.W. Lee, M. Kim, S.W. Kang, S.W. Han, *Chem. Commun.* 47 (2011) 2553–2555.
- [37] A.-J. Wang, F.-F. Li, J.-N. Zheng, H.-X. Xi, Z.-Y. Meng, J.-J. Feng, *RSC Adv.* 3 (2013) 10355–10362.
- [38] B. Lim, H. Kobayashi, T. Yu, J. Wang, M.J. Kim, Z.-Y. Li, M. Rycenga, Y. Xia, *J. Am. Chem. Soc.* 132 (2010) 2506–2507.
- [39] X.-R. Li, X.-L. Li, M.-C. Xu, J.-J. Xu, H.-Y. Chen, *J. Mater. Chem. A* 2 (2014) 1697–1703.
- [40] F. Li, Y. Guo, R. Li, F. Wu, Y. Liu, X. Sun, C. Li, W. Wang, J. Gao, *J. Mater. Chem. A* 1 (2013) 6579–6587.
- [41] Y.W. Lee, M. Kim, Z.H. Kim, S.W. Han, *J. Am. Chem. Soc.* 131 (2009) 17036–17037.
- [42] H. Zhang, X. Xu, P. Gu, C. Li, P. Wu, C. Cai, *Electrochim. Acta* 56 (2011) 7064–7070.
- [43] Y. Li, W. Gao, L. Ci, C. Wang, P.M. Ajayan, *Carbon* 48 (2010) 1124–1130.
- [44] J.-J. Feng, H. Guo, Y.-F. Li, Y.-H. Wang, W.-Y. Chen, A.-J. Wang, *ACS Appl. Mater. Interfaces* 5 (2013) 1226–1231.
- [45] Y. Zhao, L. Zhan, J. Tian, S. Nie, Z. Ning, *Electrochim. Acta* 56 (2011) 1967–1972.
- [46] H.-L. Guo, X.-F. Wang, Q.-Y. Qian, F.-B. Wang, X.-H. Xia, *ACS Nano* 3 (2009) 2653–2659.
- [47] J. Lee, S. Shim, B. Kim, H.S. Shin, *Chem. Eur. J.* 17 (2011) 2381–2387.
- [48] C. Xu, X. Wang, J. Zhu, *J. Phys. Chem. C* 112 (2008) 19841–19845.
- [49] S. Sharma, A. Ganguly, P. Papakonstantinou, X. Miao, M. Li, J.L. Hutchison, M. Delichatsios, S. Ukleja, *J. Phys. Chem. C* 114 (2010) 19459–19466.
- [50] C. Hu, Y. Zhao, H. Cheng, Y. Hu, G. Shi, L. Dai, L. Qu, *Chem. Commun.* 48 (2012) 11865–11867.
- [51] X. Liu, G. Fu, Y. Chen, Y. Tang, P. She, T. Lu, *Chem. Eur. J.* 20 (2014) 585–590.
- [52] S. Zhang, Y. Shao, G. Yin, Y. Lin, *Angew. Chem. Int. Ed.* 49 (2010) 2211–2214.
- [53] L. Kuai, B. Geng, S. Wang, Y. Sang, *Chem. Eur. J.* 18 (2012) 9423–9429.
- [54] Y. Li, Z.W. Wang, C.-Y. Chiu, L. Ruan, W. Yang, Y. Yang, R.E. Palmer, Y. Huang, *Nanoscale* 4 (2012) 845–851.
- [55] C. Xu, Y. Liu, Q. Hao, H. Duan, *J. Mater. Chem. A* 1 (2013) 13542–13548.
- [56] S.-S. Li, J. Yu, Y.-Y. Hu, A.-J. Wang, J.-R. Chen, J.-J. Feng, *J. Power Sources* 254 (2014) 119–125.
- [57] Z.-Y. Shih, C.-W. Wang, G. Xu, H.-T. Chang, *J. Mater. Chem. A* 1 (2013) 4773–4778.
- [58] W. Zhou, J.Y. Lee, *Electrochem. Commun.* 9 (2007) 1725–1729.
- [59] Z.-Y. Zhou, Z.-Z. Huang, D.-J. Chen, Q. Wang, N. Tian, S.-G. Sun, *Angew. Chem. Int. Ed.* 49 (2010) 411–414.
- [60] S.W. Lee, S. Chen, W. Sheng, N. Yabuuchi, Y.-T. Kim, T. Mitani, E. Vescovo, Y. Shao-Horn, *J. Am. Chem. Soc.* 131 (2009) 15669–15677.